ADVANCED OPTICAL MATERIALS

www.advopticalmat.de

Plasmonic Metasurfaces with High UV–Vis Transmittance for Photopatterning of Designer Molecular Orientations

*Hao Yu, Miao Jiang, Yubing Guo, Taras Turiv, Wu Lu, Vishva Ray, Oleg D. Lavrentovich, and Qi-Huo Wei**

Recent developments of utilizing plasmonic metasurfaces in photopatterning of designer molecular orientations have facilitated numerous new applications of liquid crystals; while the optical efficiency of the metamasks remains a critical issue, especially in the UV region. Here a new design of plasmonic metasurfaces made of parallelepiped arrays is presented which yield very high and broadband transmission in the UV–vis wavelength range. It is shown that this plasmonic metamask exhibits two polarization peaks originated from a cavity mode and lattice resonance respectively and demonstrated that complex designer molecular orientations can be photopatterned by using this metamask with significantly reduced exposure time. This type of high-efficiency broadband plasmonic metasurfaces is not only important for high resolution photopatterning of molecular orientation but also tailorable for various other flat optics applications in the UV and near UV regions.

Liquid crystals are not only an intriguing subject of soft matter physics but also crucial materials for many distinctive applications such as flat panel displays.[1,2] A variety of emerging applications become possible when spatially variant molecular orientation (also called molecular director) can be controlled at will. For example, liquid crystal Pancharatnam–Berry phase optical elements such as Q-plates, lenses, and beam shapers can be made to modify the orbital angular momentum, propagation direction, and intensity profiles of light beams.[3–8] The stimulus-responsive deformations of liquid crystal elastomers can be preprogrammed in molecular director patterns, promising various applications in actuators and origami-inspired surfaces.[9–14] Liquid crystals with predesigned molecular director fields can enable controlling colloidal placements and assembly,[15] nonlinear electrokinetic flows,[16] and commanding active matter like swimming bacteria.[17]

As the molecular director in bulk liquid crystals is set primarily by its condition at the bounding surfaces,[1] proper molecular alignment at surfaces is an essential step in liquid crystal device manufacturing.[18] Early applications and efforts were focused on uniform alignment,[18–20] while the emerging applications described above have driven rapid developments of techniques for aligning liquid crystal molecules into spatially variant directors. These techniques are based either on maskless approaches such as interference photoalignment[21] and pixel-to-pixel direct writing,[12,22,23] or on mask-based approaches such as using digital micromirror devices as a dynamic mask.[24,25]

More recently, Guo et al. developed a technique for photopatterning molecular orientations by using engineered plasmonic metamasks (PMMs), in a fashion similar to projection photolithography.[26] In contrast to traditional photomasks in photolithography which generate only light intensity patterns, the PMMs generate spatially variant patterns of polarization directions.[26] Projecting such polarization patterns onto thin films of photoalignment materials leads to reorientation of the rod-shaped molecules according to the molecular director patterns encoded in the polarization patterns of the PMMs, which can then be imposed onto liquid crystals confined by these substrates.[26] This PMM-based photopatterning significantly increases the spatial resolution and throughput in controlling molecular orientations and has facilitated various exciting new applications.[8,13,15–17,27,28] However, the existing design of the PMMs suffers from low optical efficiency in the near UV wavelengths, and PMMs with high optical transmittance are still needed to match the absorption bands of various photoalignment materials.

Metasurfaces based on plasmonic and dielectric materials exhibit extraordinary capabilities in controlling the amplitude and phase profiles with subwavelength spatial resolutions.[29–38] However, efficient and robust metasurfaces working in the UV

H. Yu, Dr. M. Jiang, Dr. Y. Guo, T. Turiv, Prof. O. D. Lavrentovich, Prof. Q.-H. Wei
Advanced Materials and Liquid Crystal Institute
Kent State University
Kent, OH 44242, USA
E-mail: qwei@kent.edu

Prof. W. Lu
Department of Electrical and Computer Engineering
Ohio State University
Columbus, OH 43210, USA

Dr. V. Ray
Lurie Nanofabrication Facility
Department of Electrical Engineering and Computer Science
University of Michigan
Ann Arbor, MI 48109, USA

Prof. O. D. Lavrentovich, Prof. Q.-H. Wei
Department of Physics
Kent State University
Kent, OH 44242, USA

The ORCID identification number(s) for the author(s) of this article can be found under https://doi.org/10.1002/adom.201900117.

DOI: 10.1002/adom.201900117

or near UV regions are still scarce,[39–43] even though they are highly desired by various applications. As pointed out by Yao and co-workers,[42] this is limited by available material properties. Common plasmonic materials like Au and Ag are not suitable for UV due to Ohmic losses;[42] UV-transparent dielectric materials suffer from low refractive indices and interband transitions. Several recent studies utilize metasurfaces as active or nonlinear devices for UV light generation through interband transitions or nonlinearity property.[39–41] The only work on wavefront engineering in the UV region is based on niobium pentoxide (Nb_2O_5).[43]

Here we present a new design of plasmonic polarization metasurfaces with very high optical transmission as the PMMs for photopatterning complex molecular directors. As schematically shown in **Figure 1**a, the new PMMs are composed of rectangular aluminum parallelepipeds arranged in a triangular lattice on a fused quartz substrate. Figure 1b,c presents representative scanning electron microscope (SEM) images of the fabricated PMMs. For convenience, we use l, w, h, p, and θ to represent the length, width, height, periodicity, and orientation of the parallelepipeds, respectively. As a tradeoff between the requirement for subwavelength periodicity and the reliability of nanofabrication processes, we fixed the periodicity p and height h at 220 and 80 nm. By using a finite-difference time-domain (FDTD) algorithm (CST Microwave Studio Suite from CST AG), we numerically study how the optical transmission and polarization contrast are affected by the parallelepiped size, aiming to maximize the optical transmission and polarization contrast in the absorption bands of photoalignment materials such as the SD-1 (see SM) and PAAD-22 from Beamco Inc.[44]

Figure 1d–g presents exemplary simulation results for parallelepiped arrays with p = 220 nm and h = 80 nm. When the incident polarization is along the short axis of the parallelepipeds (i.e., x-axis), the optical transmittance T_x increases monotonically with the wavelength for $\lambda > 350$ nm and can reach >80% for the i-line wavelength (365 nm). By contrast, when the incident polarization is along the long axis of the parallelepipeds (i.e., y-axis), the optical transmittance T_y is low in the wavelength range between ≈350 and ≈550 nm. Overall the polarization-dependent optical transmissions yield a polarization contrast T_x/T_y above 10 with two peaks around 350 and 450 nm, respectively.

The variations of the optical transmittance and the polarization contrast with the parallelepiped size are complex. As seen from Figure 1d,e, the left polarization peak at ≈350 nm is only slightly affected by the variations l, while the right polarization peak shifts to long wavelengths when l is increased or when w is decreased. The optical transmittance T_x goes up when w is decreased, but is little affected by the variation of l.

The variation of θ exerts only little impact on T_x and T_x/T_y. Figure 1f,g indicate that when θ is varied between 0° and 30°, T_x changes by less than 10%, and the polarization peaks shift by less than 10% of the peak wavelengths. To note, the PMM configurations with $\theta > 30°$ are equivalent to these with $0° < \theta < 30°$ due to the sixfold rotational symmetry of the triangular lattice. This minimal θ dependence is an important feature for the PMM as a robust metamask to generate complex polarization patterns.

To validate the simulation results, we fabricated the PMMs with different parallelepiped sizes and uniform orientations and measured their optical transmissions by using a CRAIC spectroscopy system. As shown in Figure 1h–k, the measured $T_x(\lambda)$ can exceed 80% at λ ≈365 nm (the i-line wavelength of mercury lamps) while exceed 90% for $\lambda > 400$ nm. The measured $T_y(\lambda)$ exhibit two dips, which yield two peaks in the polarization contrast spectra. Also, the position of the left polarization peak remains little changed with the variations of l and w, while the right peak shifts to longer wavelengths when l (or w) is increased (or decreased) (Figure 1h,i). Further, the optical transmittance and polarization contrast also show a robust reliability with regards to the variation of θ (Figure 1j,k). These experimental results are in good agreements with the simulations as described above (Figure 1d–g).

The efficiency of the metamasks is determined primarily by the optical transmittance T_x for polarization along the short axes of the parallelepipeds. For PMMs with uniform orientations, the transmission spectra are similar to those of the wire grid polarizers. This is somewhat expected as the arrays of parallelepipeds can be considered as a result of cutting the Al wires. Cutting the wires into rectangular parallelepipeds leads to two dips on T_y (Figure 1d–g). To elucidate the physical origins behind these dips in T_y or peaks in the polarization contrast T_x/T_y, we extract the peak wavelengths and plot them as a function of the parallelepiped length l and width w (**Figure 2**a). We can see that the left peak position of polarization spectrum is minimally affected by w (for small w) but increases with the increase of l. The right peak shifts to longer wavelength when l increased and/or w is decreased.

We calculated the spectra of the electrical field inside the gap between two neighboring parallelepipeds and find that there exists a resonant peak in the near field spectra at the wavelength of the left polarization peak (Figure 2b) and a standing wave is formed within the gap (Figure 2c). This indicates that the left polarization peak originates from a cavity resonance mode related to standing waves formed by the gap surface plasmons, and thus the variation with l and insensitivity with w of the left polarization peak are related to the dispersion dependence of the gap surface plasmon on gap size. The results for other orientation angles θ are similar (see Figure S2 of the Supporting Information with $\theta = 30°$).

The local electric fields at right peak wavelength also exhibit localizations within the air gap (Figure 2d), while no peak is observed in the near field spectra (Figure 2b). Again, the same is observed for nonzero orientation angle θ (Figure S2, Supporting Information). We attribute the right polarization peak to a plasmonic lattice resonance.[45] The parallelepipeds can be treated as electrical dipoles and the dipole moment for the ith parallelepiped can be written as $P_i = \alpha_0 \cdot E_i$, where α_0 is the polarizability of individual parallelepiped, and the electric field E_i acting on the dipole is the sum of the incident field E_0 and the electrical fields generated by the other dipoles. It can be shown that under perpendicular illumination, $P_i = \dfrac{\alpha_0}{1-\alpha_0 S} E_0$, where $S = \sum_{i \neq j} \left[\dfrac{(1 - ikr_{ij})\left(3\cos^2\theta_{ij} e^{ikr_{ij}}\right)}{r_{ij}^3} + \dfrac{k^2 \sin^2\theta_{ij} e^{ikr_{ij}}}{r_{ij}} \right]$.[45–47] A lattice resonance occurs when $\mathrm{Re}(1 - \alpha_0 S) = 0$. It can be shown that the S-parameter and thus the resonant wavelength is insensitive to the variation of θ (see SM), which explains the robustness

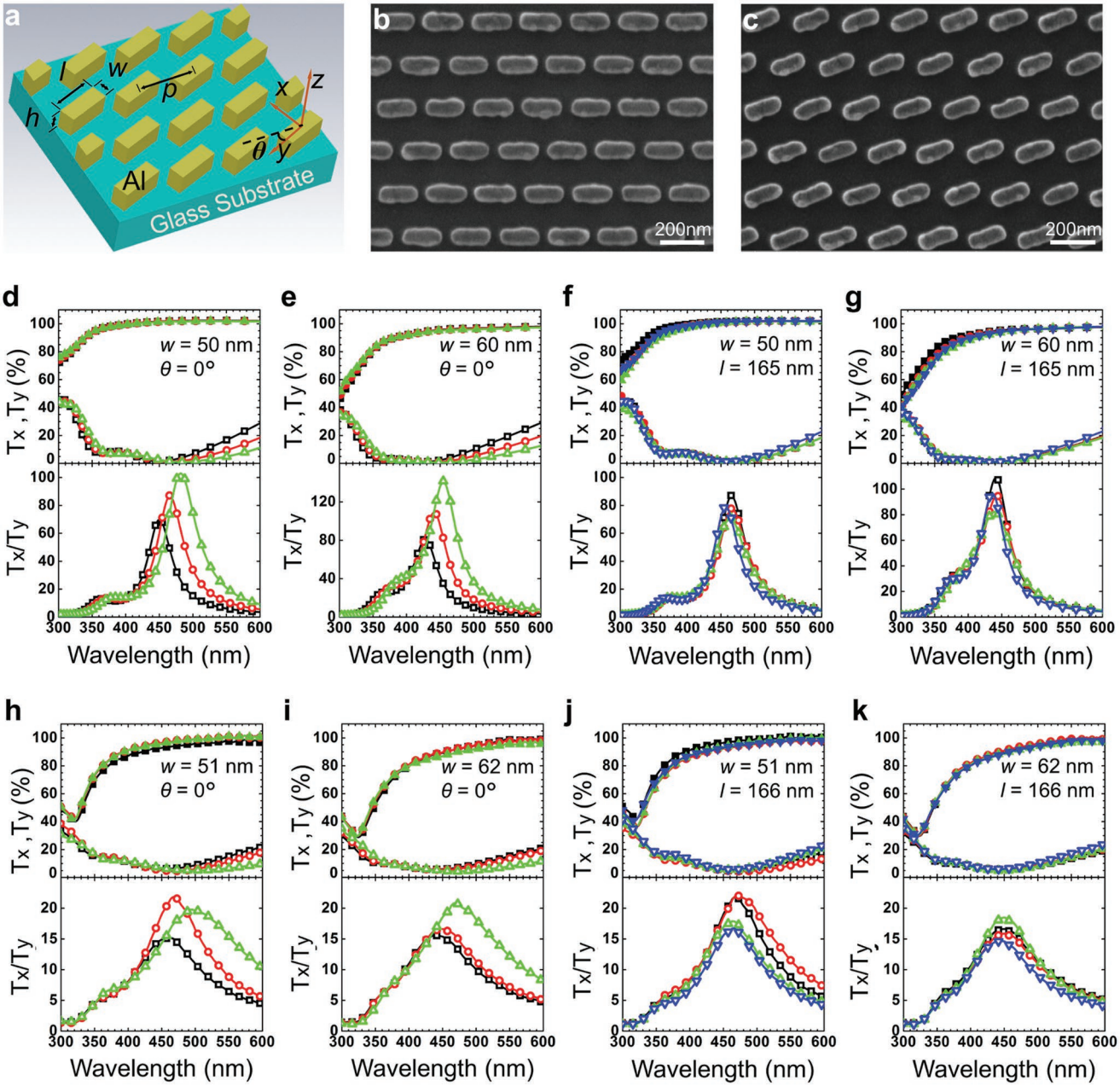

Figure 1. Simulation and experimental results for the PMM with uniform orientation. a) Schematic PMM comprised of rectangular aluminum parallelepipeds arranged in a triangular lattice. b,c) SEM images of two representative PMMs with $\theta = 0°$ in (b) and 20° in (c). d,e) Simulated optical transmittance (top) and polarization contrast (bottom) for $l = 155$ nm (black squares), 165 nm (red circles), 175 nm (green triangles), $w = 50$ nm in (d) and 60 nm in (e), and $\theta = 0°$. f,g) Simulated optical transmittance and polarization contrast for $\theta = 0°$ (black squares), 10° (red circles), 20° (green up triangles), 30° (blue down triangles), $w = 50$ nm in (f) and 60 nm in (g), and $l = 165$ nm. h,i) Measured optical transmittance (top) and polarization contrast (bottom) for $l = 156$ nm (black squares), 166 nm (red circles), 175 nm (green triangles), $w = 51$ nm in (h) and 62 nm in (i), and $\theta = 0°$. j,k) Measured optical transmittance and polarization contrast for $\theta = 0°$ (black squares), 10° (red circles), 20° (green up triangles), 30° (blue down triangles), $w = 51$ nm in (j) and 62 nm in (k), and $l = 166$ nm.

of the right polarization peak. The variation of the right peak wavelength with w and l can also be explained as related to the dependence of α_0 on the size of individual parallelepipeds.

To elucidate the capability of the PMMs in generating spatially variant polarizations, we simulated parallelepipeds forming arrays of +1/2 and −1/2 defects and calculated the electrical field distribution and polarization direction at the wavelengths of the two polarization contrast peaks (**Figure 3**a–d). Each simulated unit cell is made of 4 square tiles, two of which are 1/2 defects and the other two are −1/2 defects. Within each subunit of a single defect, the orientation θ of the parallelepipeds is set as a linear function of the azimuthal angle

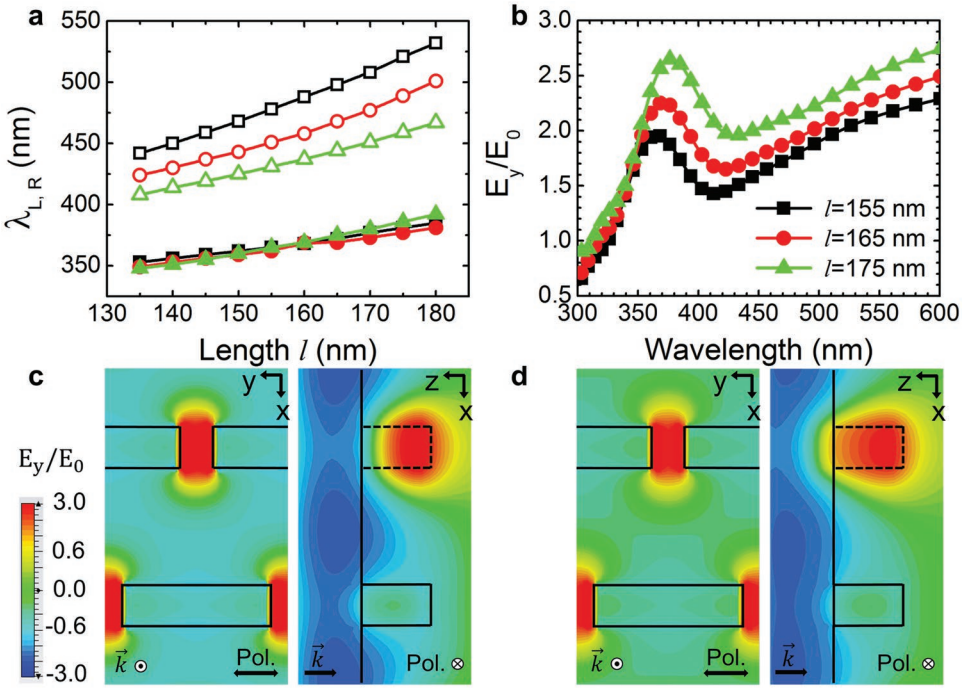

Figure 2. a) Calculated center wavelengths of the left (solid data points) and right (open data points) peaks in the polarization contrasts versus the parallelepiped length l for different parallelepiped widths: w = 40 nm (black squares), 50 nm (red circles), and 60 nm (green triangles). Here $\theta = 0°$. b) Calculated local electric field enhancement as a function of wavelength at the top center of the gap between two neighboring parallelepipeds. Here p, h, and θ are fixed at 220 nm, 80 nm, and 0°, respectively. c,d) Snapshots of the local electrical field distributions, at two resonant wavelengths, (c) 375 nm and (d) 480 nm, respectively. The incident polarization is along the y-axis, and l = 180 nm, h = 80 nm, w = 50 nm, p = 220 nm, $\theta = 0°$.

φ, $\theta = k\varphi + \psi_0$, where k is either 1/2 or −1/2, and ψ_0 is a constant. We can see that same as the PMMs with uniform orientation, the electrical fields are localized and enhanced within the cavities between two neighboring parallelepipeds (Figure 3a,b). Figure 3c,d presents calculated polarization orientations and contrasts. The spatially variant polarization orientations of the transmitted light are primarily along the short axes of the local parallelepipeds. The polarization contrast is higher than five over most regions, which is sufficient for photoalignments. Meanwhile there exist polarization contrast minima, primarily at the defect centers, which is expected as the polarization directions at these places are ill defined. This example demonstrates that this new PMM design provides simple design rule and robust control of polarization patterns.

To illustrate the performance of the new PMMs in photopatterning designer molecular directors, we designed a PMM containing a pair of +1/2 and −1/2 topological defects. Topological defects in liquid crystals represent singularities in the molecular director fields and exhibit large gradient of the director field near the defect centers, thus they can serve as challenging testbeds for the capability and spatial resolution limit of the PMM-based photopatterning. For the ±1/2 defect pair, the molecular director at (x, y) is expressed as: $\theta(x,y) = \frac{1}{2}\tan^{-1}\left(\frac{y-y_{10}}{x-x_{10}}\right) - \frac{1}{2}\tan^{-1}\left(\frac{y-y_{20}}{x-x_{20}}\right) + \frac{\pi}{2}$, where (x_{10},y_{10}) and (x_{20},y_{20}) are the center coordinates of the 1/2 and −1/2 defects, respectively. We set the orientations of the long axes of the rectangular parallelepipeds in the PMM the same as these target molecular orientations.

A representative SEM image of the fabricated pair of +1/2 (left) and −1/2 (right) defects in the PMM is shown in Figure 3e. Nonpolarized optical microscopic image of the PMM shows that the optical transmission is highly uniform (Figure 3f, upper). When the plasmonic metamask is illuminated with polarized light and observed with a cross-polarization analyzer, polarizing optical microscope (POM) image show nonuniform intensity distribution (Figure 3f, lower). Considering the metamask as a polarizer with a spatially variant polarization direction, one can expected that the pixel intensity is ~$\sin^2\gamma\cos^2\gamma$ with γ being the polarization orientation with respect to the polarizer. By illuminating the PMM with nonpolarized light and taking images of the PMM with a polarization analyzer, we can determine the polarization direction $\theta_0(x,y)$ at the pixel (x, y) by fitting the pixel intensity $I(x, y)$ versus the analyzer orientation θ with the function $I(x,y) \sim \sin^2[\theta - \theta_0(x,y)]$. The measured polarization directions are perpendicular to the long axes of the local parallelepipeds in the PMM (Figure 3g), which is in agreement with the design expectation.

The photopatterning of molecular orientations by using the PMM is done with a home-made projection photopatterning system (Figure S4, Supporting Information).[26] Basically, the PMM is illuminated with broad-band nonpolarized light, and the transmitted light becomes polarized with spatially nonuniform polarization orientation. The transmitted light is then projected onto substrates coated with photoalignment material such as SD-1. Illumination of polarized light causes the rod-shaped SD-1 molecules to reorient themselves to have their dipoles (i.e., long molecular axes) perpendicular

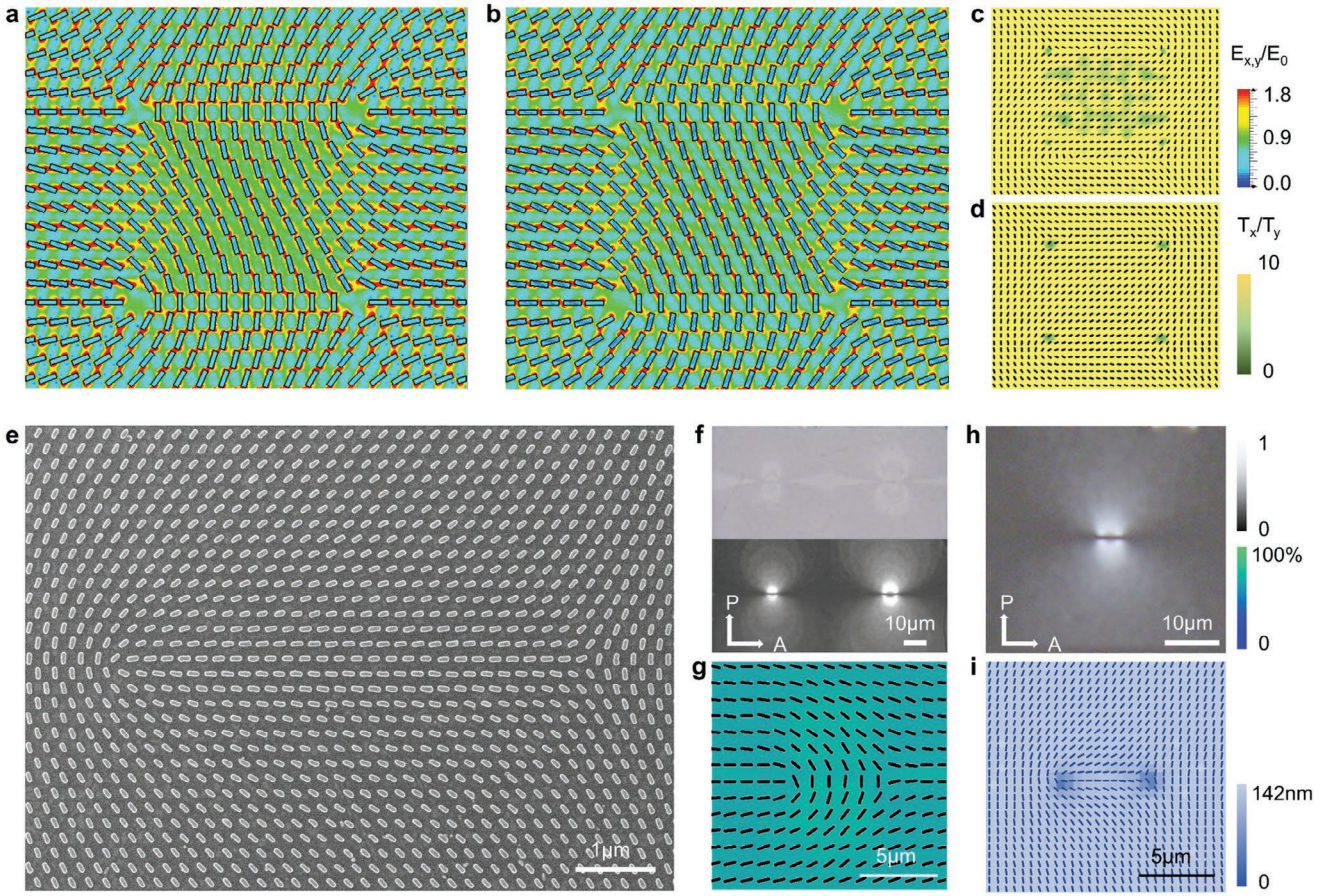

Figure 3. Simulations and photopatterning for PMMs with spatially variant polarizations. a–d) Simulated near field distribution and polarization orientation at the peak wavelength $\lambda = 375$ (a,c) and the peak wavelength $\lambda = 480$ nm (b,d). The parallelepiped size and period: $l = 180$ nm, $h = 80$ nm, $w = 50$ nm, and $p = 220$ nm. The calculated electrical field is at a plane 420 nm above the parallelepipeds. e) A SEM image of the PMM with a ±½ defect pair. f) Transmission optical microscopic images without (top) and with crossed polarizers (bottom) for the fabricated PMM with two pairs of ±½ defects, the defect spacing is 6 and 8 μm, respectively. g) Measured polarization pattern for the PMM, where the background color represents the optical transmittance. h,i) POM and PolScope images of an LC polymer sample photopatterned with the PMM with one defect pair, where blue lines represent molecular orientation and background color the local phase retardation. Arrows P and A in (f) and (h) represent the orientation of polarizer and analyzer in POM. The color scale bars, from top to bottom on the right side, represent local field enhancements, polarization contrast (T_x/T_y), the optical transmittance and phase retardation in (a,b), (c,d), (g), and (i), respectively. The gray scale bar represents normalized light intensity for individual pixels for (f, bottom).

to the polarization directions. As a result, the polarization pattern is converted into the orientation pattern of the SD-1 molecules. When other liquid crystal molecules such as RM-257 are spin-coated on the SD-1 films, they will follow the orientations of the SD-1 due to molecular interactions. This process is very similar to the projection photolithography except that the PMM generates polarization patterns instead of intensity patterns and the photoexposure cause molecular reorientation instead of photochemical reactions (leading to microstructures).

Figure 3h,i represents polarized microscopic and PolScope images of a sample of liquid crystal polymers fabricated according to the photopatterning processes described in the Experimental Session. It can be seen that the molecular orientations are the same as those of the parallelepipeds in the PMM in Figure 3e and that the phase retardation is highly uniform, demonstrating its high performances in photopatterning and in-plane alignment of the LC molecules. This also demonstrates extremely simple design rules to the PMMs, i.e., orienting the parallelepipeds according exactly to desired molecular orientations.

To quantify the performance of the new PMM in photopatterning, we did dose tests to compare this new parallelepiped-based PMMs with the prior nanoaperture-based PMMs (**Figure 4**). The optical transmissions of the nanoaperture-based PMMs are primarily located at wavelengths above 400 nm (see SM, Figure S5, Supporting Information). When the X-Cite 120 light source is used at its maximal intensity output and the projection system works at 1:1 magnification, the required exposure time is less than 1 s for both types of PMMs. Therefore, to facilitate an accurate comparison, we used the lowest output intensity of the light source and set projection magnification to 2.5. Figure 4a,b and Figure. 4e,f present POM and PolScope images of polymerized RM-257 films on SD-1 photopatterned with the new PMM; and Figure 4c,d and Figure 4g,h present the POM and PolScope images of polymerized RM-257 films

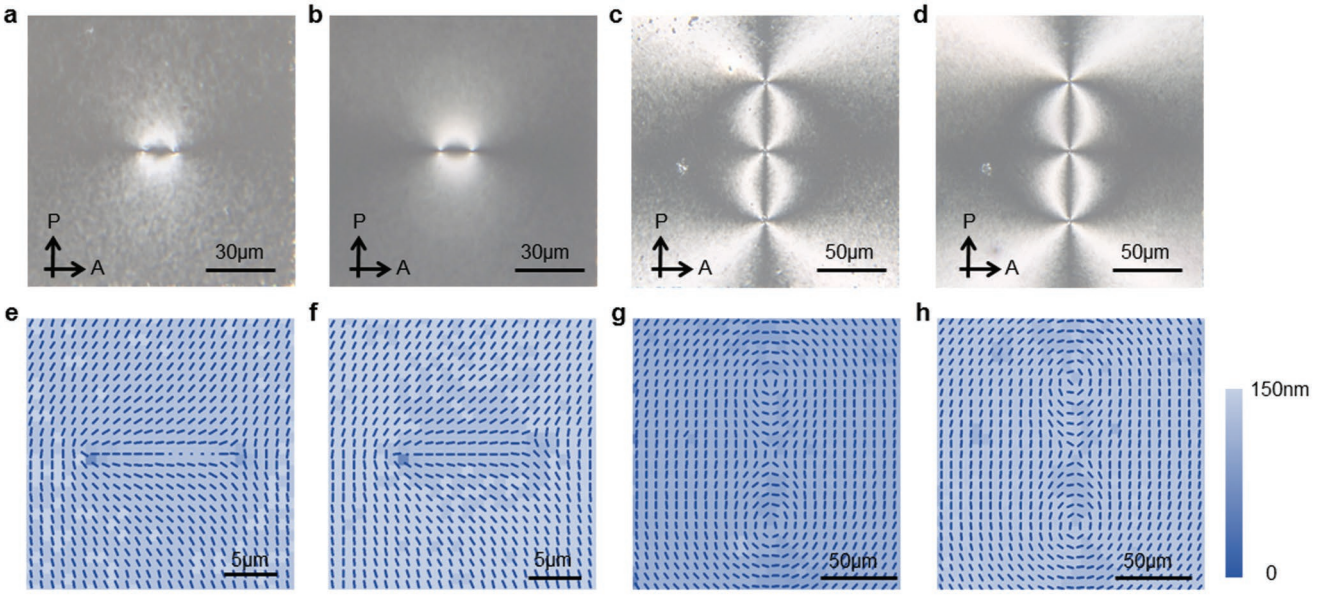

Figure 4. A comparison of exposure time between the parallelepiped-based and prior nanoaperture-based PMMs. a–d) Representative POM images of the LC films photopatterned with the parallelepiped-based PMMs with: (a) 10 s and (b) 20 s exposure times, and the nanoaperture-based PMM with: (c) 70 s and (d) 80 s exposure time. e–h) Corresponding Polscope images of the photopatterned LC films in (a–d), where the background color represents phase retardation and the lines represent molecular orientations. A and P in (a–d) indicate the orientations of the polarizer and analyzer in the microscope.

on SD-1 photopatterned with a prior PMM based on rectangular hole arrays in Al films. The noises in the polarizing optical microscope images in Figure 4a–d indicate that the liquid crystal molecules are not fully aligned, and that the degree of alignments fluctuates spatially. The phase retardation measured by the PolScope is defined as $\delta = (n_e - n_o)t$, where n_e, and n_o, are the refractive index for polarization parallel and perpendicular the molecular axis, and t is the film thickness. When all molecular are all aligned, $(n_e - n_o)$ maximizes. Therefore, longer exposure times lead to less noises in the POM images and larger phase retardations, or higher degrees of molecular alignments.

Under the same illumination intensity and projection magnification, we found that at least 80 s is needed for the old nanoaperture-based PMMs to achieve smooth molecular orientation patterns (Figure 4d,h). By contrast, the parallelepiped-based PMM only needs 20 s (Figure 4b,f). This demonstrates that a significant reduction (≈75%) in the exposure time is achieved by using the new PMMs.

In conclusion, we have demonstrated that plasmonic metasurfaces consisting of arrays of Al rectangular parallelepipeds can serve as UV metamasks for photopatterning of designer molecular orientations with very high optical efficiency. By numerical simulations, we show that such plasmonic metamasks exhibit two peaks in their polarization contrast spectra due respectively to the cavity and lattice resonances and that the central wavelengths of these two peaks are minimally affected by varying the parallelepiped orientation, making them very robust in polarization control. We show that photopatterning with this new type of metamasks significantly reduce the exposure time. Though not shown here, it can also be expected that photopatterning with UV light can increase its spatial resolution. Further, we like to point out that the Al-based metasurfaces are actually quite stable overtime, because the thin aluminum oxide on the Al surfaces is able to protect Al from further oxidation.

It is important to note that the optical efficiency of the Al parallelepiped metasurfaces is equivalent to that of dielectric metasurfaces. In comparison to the high aspect ratios (≈10:1) required by dielectric metasurfaces, the low aspect ratio of the parallelepipeds (≈1:1) make the Al metasurface easy to fabricate. In addition, though the data presented in this paper are for fixed parallelepiped height and periodicity, we did simulations with other heights and periodicities and observed that by varying the size of the parallelepipeds, the polarization peaks can be further tuned at least down to 300 nm. It can be expected that such Al plasmonic metasurfaces find many applications in flat optics in the UV region, including metalenses, metaholograms, and metagratings.

Experimental Section

Numerical Simulations: The optical properties of the PMMs were numerically modeled by using the commercial software CST MICROWAVE STUDIO. Hexahedral mesh scheme was used with small mesh sizes (≤10 nm, much smaller than the surface resonance wavelength). The thickness of the fused quartz substrate was set as infinity, and the size (length, width, and height) and periodicity of the parallelepipeds were varied according to the designs. The PMMs were illuminated from the quartz substrates side. The distributions of the electrical and magnetic fields at a plane of 420 nm above the PMM were collected to calculate the transmission spectra.

Fabrication of the PMMs: A 80 nm Al film and a 40 nm SiO_2 film were sequentially deposited on fused quartz substrates by sputtering deposition, then a 100 nm Al film was deposited and patterned to cover the SiO_2 film except the areas for the PMM patterns by

photolithography, Al deposition, and a lift-off process. These substrates were then spin-coated with e-beam resist and patterned with e-beam writing. After resist development, a 25 nm Al film was deposited and lift-off, the mask patterns were then transferred into the SiO_2 layers and then to the Al layer through reactive ion etching.

Projection Photopatterning System: An optical setup was home-built for projection photopatterning liquid crystal molecular orientations, and details were published in a prior paper.[26] A schematic of the setup is shown in Figure S4 of the Supporting Information. A nonpolarized white light source, the X-Cite series 120, is used to illuminate the PMMs. After passing through the PMMs, light with spatially variant polarization patterns is generated and then collected by an NUV imaging objective (obj1) and projected onto the glass substrate coated with photoalignment materials by using the projection objective (obj2). The magnification of the projection setup is determined by the ratio between the magnifications of the imaging objective and projection objective.

Photopatterning Process: Cleaned glass slides were spin-coated with sulfuric dye 1 (SD-1, 0.4 wt% in dimethylformamide) with a 3000 rpm spin speed and then baked on a hot plate at 85 °C for 20 min. These glass slides with coated SD-1 films were exposed by using the projection photopatterning system, with the exposure time depending on the light intensity of light source and the magnification. On these slides with photopatterned SD-1, toluene solutions of the LC Monomer RM257 (10 wt%) and Irgacure 651 photoinitiator (5 wt% of RM257) were spin-coated to at 3000 rpm for 40 s. After a 15 min photopolymerization with UV illumination, the photopatterned orientations of the SD-1 molecules were transferred to the RM257 molecules and then fixed by photopolymerization process.

Optical Characterization: The PolScope technique is used to accurately map out the molecular orientation in patterned LC films. The PolScope illuminates samples with a monochromatic polarized light ($\lambda = 546$ nm) at different polarization orientations and allows for measuring spatially variant optical retardance and slow axis of birefringent materials.[48] For nematic LC materials with positive Δn, the slow axis is simply the long axis of the rod-shaped LC molecules.

Supporting Information

Supporting Information is available from the Wiley Online Library or from the author.

Acknowledgements

H.Y. and M.J. contributed equally to this work. This work was supported by the NSF through CMMI-1663394 and CMMI-1436565. Q.-H.W. also acknowledges the financial support by the AvH foundation and Clemens Bechinger for his hospitality of during his sabbatical in Univ. Konstanz when this manuscript was prepared.

Conflict of Interest

The authors declare no conflict of interest.

Keywords

liquid crystals, nanomanufacturing, photoalignments, plasmonic metasurfaces, topological defects

Received: January 18, 2019
Revised: March 1, 2019
Published online: March 25, 2019

[1] P. G. de Gennes, J. Prost, *The Physics of Liquid Crystals*, Clarendon Press, New York **1993**.
[2] D.-K. Yang, S.-T. Wu, *Fundamentals of Liquid Crystal Devices*, John Wiley & Sons, Ltd, Chichester, UK **2014**.
[3] L. Marrucci, C. Manzo, D. Paparo, *Appl. Phys. Lett.* **2006**, *88*, 221102.
[4] K. Gao, H.-H. Cheng, A. Bhowmik, C. McGinty, P. Bos, *Appl. Opt.* **2016**, *55*, 1145.
[5] C. Oh, M. J. Escuti, *Opt. Lett.* **2008**, *33*, 2287.
[6] L. De Sio, D. E. Roberts, Z. Liao, J. Hwang, N. Tabiryan, D. M. Steeves, B. R. Kimball, *Appl. Opt.* **2018**, *57*, A118.
[7] J. Kim, Y. Li, M. N. Miskiewicz, C. Oh, M. W. Kudenov, M. J. Escuti, *Optica* **2015**, *2*, 958.
[8] M. Jiang, H. Yu, X. Feng, Y. Guo, I. Chaganava, T. Turiv, O. D. Lavrentovich, Q.-H. Wei, *Adv. Opt. Mater.* **2018**, *6*, 1800961.
[9] T. J. White, D. J. Broer, *Nat. Mater.* **2015**, *14*, 1087.
[10] M. E. McConney, A. Martinez, V. P. Tondiglia, K. M. Lee, D. Langley, SmalyukhII, T. J. White, I. I. Smalyukh, T. J. White, *Adv. Mater.* **2013**, *25*, 5880.
[11] L. T. De Haan, V. Gimenez-Pinto, A. Konya, T.-S. S. Nguyen, J. M. N. N. Verjans, C. Sánchez-Somolinos, J. V. Selinger, R. L. B. B. Selinger, D. J. Broer, A. P. H. J. H. J. Schenning, *Adv. Funct. Mater.* **2014**, *24*, 1251.
[12] T. H. Ware, M. E. McConney, J. J. Wie, V. P. Tondiglia, T. J. White, *Science* **2015**, *347*, 982.
[13] G. Babakhanova, T. Turiv, Y. Guo, M. Hendrikx, Q.-H. Wei, A. P. H. J. H. J. Schenning, D. J. Broer, O. D. Lavrentovich, *Nat. Commun.* **2018**, *9*, 456.
[14] H. Aharoni, Y. Xia, X. Zhang, R. D. Kamien, S. Yang, *Proc. Natl. Acad. Sci. USA* **2018**, *115*, 7206.
[15] C. Peng, T. Turiv, Y. Guo, S. V. Shiyanovskii, Q.-H. Wei, O. D. Lavrentovich, *Sci. Adv.* **2016**, *2*, e1600932.
[16] C. Peng, Y. Guo, C. Conklin, J. Viñals, S. V. Shiyanovskii, Q.-H. Wei, O. D. Lavrentovich, *Phys. Rev. E* **2015**, *92*, 052502.
[17] C. Peng, T. Turiv, Y. Guo, Q.-H. Wei, O. D. Lavrentovich, *Science* **2016**, *354*, 882.
[18] K. Takatoh, M. Sakamoto, R. Hasegawa, M. Koden, N. Itoh, M. Hasegawa, *Alignment Technology and Applications of Liquid Crystal Devices*, CRC Press, London **2005**.
[19] Vladimir G. Chigrinov, Vladimir M. Kozenkov, H.-S. Kwok, Vladimir G. Chigrinov, Vladimir M. Kozenkov, H.-S. Kwok, V. G. Chigrinov, V. M. Kozenkov, H.-S. Kwok, *Photoalignment of Liquid Crystalline Materials: Physics and Applications*, John Wiley & Sons Ltd., West Sussex, England **2008**.
[20] O. Yaroshchuk, Y. Reznikov, *J. Mater. Chem.* **2012**, *22*, 286.
[21] T. Du, F. Fan, A. M. W. Tam, J. Sun, V. G. Chigrinov, H. Sing Kwok, *Adv. Mater.* **2015**, *27*, 7191.
[22] M. N. Miskiewicz, M. J. Escuti, *Opt. Express* **2014**, *22*, 12691.
[23] B. S. Murray, R. A. Pelcovits, C. Rosenblatt, *Phys. Rev. E* **2014**, *90*, 52501.
[24] C. Culbreath, N. Glazar, H. Yokoyama, *Rev. Sci. Instrum.* **2011**, *82*, 126107.
[25] H. Wu, W. Hu, H. Hu, X. Lin, G. Zhu, J.-W. Choi, V. Chigrinov, Y. Lu, *Opt. Express* **2012**, *20*, 16684.
[26] Y. Guo, M. Jiang, C. Peng, K. Sun, O. Yaroshchuk, O. Lavrentovich, Q.-H. Wei, *Adv. Mater.* **2016**, *28*, 2353.
[27] C. Peng, Y. Guo, T. Turiv, M. Jiang, Q.-H. Wei, O. D. Lavrentovich, *Adv. Mater.* **2017**, *29*, 1606112.
[28] M. Jiang, Y. Guo, H. Yu, Z. Zhou, T. Turiv, O. D. Lavrentovich, Q.-H. Wei, *Adv. Mater.* **2019**, https://doi.org/10.1002/adma.201808028.
[29] N. Yu, P. Genevet, M. A. Kats, F. Aieta, J.-P. Tetienne, F. Capasso, Z. Gaburro, *Science* **2011**, *334*, 333.
[30] Y. Zhao, A. Alù, *Phys. Rev. B* **2011**, *84*, 205428.
[31] X. Ni, N. K. Emani, A. V Kildishev, A. Boltasseva, V. M. Shalaev, *Science* **2012**, *335*, 427.

[32] D. Lin, P. Fan, E. Hasman, M. L. Brongersma, *Science* **2014**, *345*, 298.
[33] R. C. Devlin, M. Khorasaninejad, W. T. Chen, J. Oh, F. Capasso, *Proc. Natl. Acad. Sci. USA* **2016**, *113*, 10473.
[34] M. Khorasaninejad, W. T. Chen, R. C. Devlin, J. Oh, A. Y. Zhu, F. Capasso, *Science* **2016**, *352*, 1190.
[35] N. Yu, F. Capasso, *Nat. Mater.* **2014**, *13*, 139.
[36] P. Genevet, F. Capasso, F. Aieta, M. Khorasaninejad, R. Devlin, *Optica* **2017**, *4*, 139.
[37] S. Wang, P. C. Wu, V.-C. Su, Y.-C. Lai, M.-K. Chen, H. Y. Kuo, B. H. Chen, Y. H. Chen, T.-T. Huang, J.-H. Wang, R.-M. Lin, C.-H. Kuan, T. Li, Z. Wang, S. Zhu, D. P. Tsai, *Nat. Nanotechnol.* **2018**, *13*, 227.
[38] G. Zheng, H. Mühlenbernd, M. Kenney, G. Li, T. Zentgraf, S. Zhang, *Nat. Nanotechnol.* **2015**, *10*, 308.
[39] M. Semmlinger, M. L. Tseng, J. Yang, M. Zhang, C. Zhang, W.-Y. Tsai, D. P. Tsai, P. Nordlander, N. J. Halas, *Nano Lett.* **2018**, *18*, 5738.
[40] S. V. Makarov, A. N. Tsypkin, T. A. Voytova, V. A. Milichko, I. S. Mukhin, A. V. Yulin, S. E. Putilin, M. A. Baranov, A. E. Krasnok, I. A. Morozov, P. A. Belov, *Nanoscale* **2016**, *8*, 17809.
[41] S. Liu, P. P. Vabishchevich, A. Vaskin, J. L. Reno, G. A. Keeler, M. B. Sinclair, I. Staude, I. Brener, *Nat. Commun.* **2018**, *9*, 2507.
[42] Y. Deng, X. Wang, Z. Gong, K. Dong, S. Lou, N. Pégard, K. B. Tom, F. Yang, Z. You, L. Waller, J. Yao, *Adv. Mater.* **2018**, *30*, 1802632.
[43] K. Huang, J. Deng, H. S. Leong, S. L. K. Yap, R. B. Yang, J. Teng, H. Liu, **2018**, arXiv:1806.03131.
[44] V. Chigrinov, H. S. Kwok, H. Takada, H. Takatsu, *Liq. Cryst. Today* **2005**, *14*, 1.
[45] F. J. García de Abajo, *Rev. Mod. Phys.* **2007**, *79*, 1267.
[46] L. Zhao, K. L. Kelly, G. C. Schatz, *J. Phys. Chem. B* **2003**, *107*, 7343.
[47] S. Zou, N. Janel, G. C. Schatz, *J. Chem. Phys.* **2004**, *120*, 10871.
[48] M. Shribak, R. Oldenbourg, *Appl. Opt.* **2003**, *42*, 3009.

